Theoretical calculation for the multiplet structures of tetrahedrally coordinated Cr^{4+} in silicate crystals

Theoretical calculation for the multiplet structures of tetrahedrally coordinated Cr^{4+} in silicate crystals

Takugo Ishii[1], Koji Fujimura[1], Kazuyoshi Ogasawara[1], Hirohiko Adachi[1] and Isao Tanaka[2]

[1] Department of Materials Science and Engineering, Kyoto University, Sakyo, Kyoto 606-8501, Japan
[2] Department of Energy Science and Technology, Kyoto University, Sakyo, Kyoto 606-8501, Japan

Abstract

The multiplet structures of tetrahedrally coordinated Cr^{4+} in the three silicate crystals Mg_2SiO_4 (forsterite), $Ca_2MgSi_2O_7$ (åkermanite), and Y_2SiO_5 (yttrium orthosilicate (YSO)) were calculated by the many-electron electronic structure calculation method developed by the authors. The method is a hybrid of the molecular orbital method based on the density functional theory and the configuration interaction approach. For every crystal, the calculations were conducted by using cluster models with the three sizes: (A) $(CrO_4)^{4-}$ (without point charges) models, (B) $(CrO_4)^{4-}$ (with point charges) models, and (C) $(CrMg_9Si_2O_{37})^{44-}$ (forsterite), $(CrCa_6Mg_2SiO_{38})^{52-}$ (åkermanite), and $(CrY_8O_{37})^{46-}$ (YSO) models. The calculated multiplet energies of the triplet states agreed with the experimentally obtained peak energies in the absorption spectra in the literature. The theoretical spectra showed polarization dependence of the peak intensity. The best agreement was found in the results obtained from the largest models C. The difference in polarization dependence between Cr^{4+}:forsterite and Cr^{4+}:åkermanite was related to the different mixing of the many-electron wave functions as regards the $^3T_2(et_2)$ and $^3T_1(et_2)$ triplet terms. The covalency of the impurity-level molecular orbitals was also analysed. The results of models C indicated that the wave functions of the atoms outside the CrO_4 tetrahedron should not be neglected. Both the degree of covalency and the correlation-correction factor, which was introduced in the method, were regarded as reduction factors of two-electron repulsion. The two factors were multiplied together, and the reduction factor was a convenient indicator for simply evaluating the magnitude of the reduction. The traditional nephelauxetic parameter was obtained as 0.49. Some empirical values given recently in the literature were confirmed to have appropriate magnitude.

1. Introduction

Cr^{4+}-doped crystals have been studied as regards their use as solid-state laser materials since the laser action in Cr^{4+}:Mg_2SiO_4 (forsterite) was first reported [1]. The history of Cr^{4+} lasers up to the present is summarized in reference [2]. It has proved difficult to understand the optical absorption spectra in the spectral region from the near-infrared (NIR) to the visible. The main source of the difficulty lay in the frameworks of the theoretical methods. Most traditional methods for the analysis of the absorption spectra produced by transition-metal impurities have been based on ligand-field theory [3], which requires one to make various assumptions in order to determine the adjustable parameters. Even if one makes an invalid assumption, one can often explain the origin of the absorption spectra by arbitrarily adjusting the parameters.

To avoid ambiguity in determining the parameters, we have to depend on *ab initio* methods. Until now, however, applications of *ab initio* electronic structure calculation methods to solid-state laser crystals have been limited, although the number of studies focused on the determination of the structure and the thermal properties of minerals has been increasing. To calculate the electronic structures of host crystals, Xu and Ching, and Xu, Ching, and Brickeen successfully conducted band calculations for garnet crystals [4,5], whose unit cells were huge, with 160 atoms. However, since the band method is based on a one-electron approximation, we cannot directly discuss the impurity states that appear as a multiplet structure, requiring a many-electron calculation. As for the multiplet structures of Cr^{4+}-doped system, Wissing *et al* and Deghoul *et al* conducted molecular orbital calculations on Cr^{4+}:forsterite and Cr^{4+}:Ca_2GeO_4, and on Cr^{4+}:$LiNbGeO_5$, respectively [6, 7]. Their procedure, however, was fundamentally based on the matrix elements obtained by the traditional ligand-field theory, which restricted the applicable symmetry. So they could give the mean energies of the multiplet terms in a hypothetical T_d symmetry, but could not obtain the energy splittings that were produced by low symmetries, which were of significant interest.

We have been developing a general *ab initio* method, the discrete variational multi-electron (DVME) method [8], for direct calculation of multiplet structures, independently of the traditional ligand-field theory. In this paper, we report the results obtained from calculations of the multiplet structures of tetrahedrally coordinated Cr^{4+} in Mg_2SiO_4 (forsterite), $Ca_2MgSi_2O_7$ (åkermanite), and Y_2SiO_5 (YSO) silicate crystals. We confirm that every polarization dependence of the peak intensity was reproduced by the calculations, without using any adjustable parameters for that purpose. From the examination of the dependence of the size of the cluster models, we show that the wave functions of the atoms outside the CrO_4 tetrahedra should always be considered when we discuss not only the peak energy but also the peak intensity. Finally, the so-called nephelauxetic parameter is calculated, and the magnitudes of some values given in the literature are validated.

2. Method

2.1. Computational procedure

First, in the computational procedure of the DVME method, a one-electron molecular orbital (MO) calculation by means of the SCAT code [9] is conducted. The method is based on the density functional theory, and the exchange potential is X_α [10], whose constant α is set at 0.7 as the standard value. We could apply other exchange potentials based on the local spin-density approximation, but it has already been confirmed that the result would be essentially the same as that obtained by using the X_α-potential [8]. The self-consistent calculation is conducted with the use of a cluster model, in which the crystal structure and the symmetry are included.

The pth MO φ_p is expressed as a linear combination of atomic orbitals χ, such as:

$$\varphi_p(r) = \sum_q c_{pq} \chi_q(r) \tag{1}$$

where r is the position of the electron, and c_{pq} is the coefficient of the linear combination. The atomic orbitals used in this study were 1s–4p for chromium (Cr), 1s–2p for oxygen (O), 1s–3d for silicon (Si), 1s–3d for magnesium (Mg), 1s–4p for calcium (Ca), and 1s–5p for yttrium (Y).

Once we have obtained the one-electron MO energy and the MO, we take only the impurity-level MOs that are mainly composed of transition-metal d orbitals, with N electrons. The ith wave function Ψ_i of the N-electron system (d^N many-electron system) is constructed as a linear combination of Slater determinants Φ, such as:

$$\Psi_i(r_1, r_2, \ldots, r_N) = \sum_{j=1}^{s} C_{ij} \Phi_j(r_1, r_2, \ldots, r_N)$$

$$\Phi_j(r_1, r_2, \ldots, r_N) = \frac{1}{\sqrt{N!}} \begin{vmatrix} \varphi_{j1}(r_1) & \varphi_{j2}(r_1) & \cdots & \varphi_{jN}(r_1) \\ \varphi_{j1}(r_2) & \varphi_{j2}(r_2) & \cdots & \varphi_{jN}(r_2) \\ \vdots & \vdots & \vdots & \vdots \\ \varphi_{j1}(r_N) & \varphi_{j2}(r_N) & \cdots & \varphi_{jN}(r_N) \end{vmatrix} \tag{2}$$

where s is the total number of Slater determinants, and C_{ij} is the coefficient of the linear combination. All the configuration interactions relating to the so-called d–d transition are fully considered. The effective Hamiltonian H_{eff} of the N-electron system is written in atomic units as

$$H_{eff}(r_1, r_2, \ldots, r_N) = \sum_{i=1}^{N} \left\{ -\frac{1}{2} \nabla_i^2 - \sum_\nu \frac{Z_\nu}{|r_i - R_\nu|} + V_0(r_i) \right\} + \sum_{i=1}^{N} \sum_{j>i}^{N} \frac{1}{|r_i - r_j|} \tag{3}$$

where the term in the first brackets is the one-electron operator term and the last term is the two-electron operator term. In the one-electron operator term, the first and the second terms express the kinetic energy and the electron–nuclei (with the atomic number Z) attractive potential for the N electrons, respectively. The potential V_0 includes the Coulomb and the exchange potentials between the N electrons and the core-and-valence electrons.

To calculate the potential V_0, the following explicit formula, proposed by Watanabe and Kamimura [11], is adopted:

$$V_0(r_i) = \int \frac{\rho_0(r)}{|r_i - r|} \, dr + \frac{3}{4} \frac{\rho_{tot}(r_i) V_{xc}[\rho_{tot}(r_i)] - \rho_0(r_i) V_{xc}[\rho_0(r_i)]}{\rho_{imp}(r_i)} - V_{xc}[\rho_{imp}(r_i)] \tag{4}$$

where ρ_{tot}, ρ_0, and ρ_{imp} are the electron densities of all of the occupied MOs, the core-and-valence MOs, and the impurity-level MOs, respectively. And the potential V_{xc} is the exchange X_α-potential. This potential V_0 analytically expresses the interelectron interaction excluding the repulsion among the N electrons. Although the explicit formula expresses well the polarization dependence of the absorption spectra, it was revealed that some overestimation of the calculated energy could not be removed. We consider that the overestimation will be reduced when we construct larger Slater determinants, including the valence MOs. In the present study, however, we introduce two approaches to correct the overestimation simply. One is the configuration-dependent correction (CDC) approach, and the other is the configuration-independent correction (CIC) approach. The CDC approach had been already introduced in our previous study [8]. In the CDC approach, we need to classify the multiplet structure into several electron configurations. In the case of the Cr^{4+} ion in T_d symmetry, the impurity levels

split into two states with e and t_2 symmetries. We can define an effective ligand-field splitting Δ_{eff} from an energy difference between the two states, such as:

$$\Delta_{\text{eff}} = \overline{\varepsilon(t_2)} - \overline{\varepsilon(e)} \tag{5}$$

where ε is the MO energy, and the overline means taking an average value when the degenerate states further split into several states in symmetry lower than T_d. Then the electron configurations are $e^m t_2^n$; $(m, n) = (2, 0), (1, 1), (0, 2)$, and their mean energies are obtained as

$$n\Delta_{\text{eff}}. \tag{6}$$

In the CDC approach, the values of the diagonal matrix elements are shifted before the diagonalization so that the mean energy of every electron configuration is consistent with equation (6). If we knew the electron configuration, the correction could be done straightforwardly within the computational procedure, without introducing any adjustable parameters for correction. Thus, the framework of the CDC approach does not destroy the *ab initio* status of the DVME method. On the other hand, the CIC approach introduces a scaling factor, by which all of the matrix elements of the one-electron operator term are universally reduced. The scaling factor affects the magnitude of the ligand-field splitting, and can be selected so as to give an energy position equivalent to that of the CDC approach. In this study, however, we selected the magnitude of the scaling factor so as to reproduce the peak position of the experimentally obtained spectra, and the constant value 0.65 was universally applied throughout the calculations. Although the scaling factor in this study was introduced as an adjustable parameter, it is introduced only to correct the overall overestimation of the calculated energy, and it does not crucially affect the calculated intensity and the polarization dependence, which are the important factors in a system with low symmetries.

The two-electron operator term in equation (3) expresses the Coulomb repulsion between N electrons in the impurity-level MOs. In the DVME method, the calculation of the two-electron integrals is done numerically, not analytically, with the use of impurity-level MOs such as:

$$C \sum_{r=1}^{\Gamma} \sum_{s>r}^{\Gamma} \varphi_i(\boldsymbol{r}_r) \varphi_j(\boldsymbol{r}_s) \frac{1}{|\boldsymbol{r}_r - \boldsymbol{r}_s|} \varphi_k(\boldsymbol{r}_r) \varphi_l(\boldsymbol{r}_s) \omega(\boldsymbol{r}_r) \omega(\boldsymbol{r}_s) \tag{7}$$

where ω is the weighted volume at each sample point $\boldsymbol{r}$, and Γ is the number of sample points. The factor C, which is not an empirical parameter, is explained shortly. The numerical procedure makes it possible to apply the method universally to any symmetry and to any electron configuration. In the case of Cr^{4+}, the actual number of combinations of integrals $\langle ij|kl \rangle$ is 140. In the traditional semiempirical methods based on the ligand-field theory, however, these integrals are usually reduced to just one adjustable Racah parameter B. At the last stage in the computational procedure of the DVME method, the energies and the wave functions of the N-electron system are obtained by diagonalization of the matrix of the effective many-electron Hamiltonian.

The Coulomb repulsion between the N electrons should be overestimated due to the insufficient consideration of the electron correlation effect, since the number of Slater determinants is finite. To include the electron correlation effect, the two-electron integrals in equation (7) are multiplied by a correlation-correction factor C, which is straightforwardly determined by a spin-polarized MO calculation. The factor C is selected so as to achieve consistency between the spin-flip transition energy $\Delta\epsilon$, calculated by a one-electron calculation within the transition-state method proposed by Slater [12], and the corresponding transition

energy ΔE, estimated by the N-electron calculation. In the case of the Cr^{4+} state in T_d symmetry, the condition is written as

$$\overline{E[^1E,\,^1A_1,\,^3A_2(e_\uparrow e_\downarrow)] - E[^3A_2(e_\uparrow^2)]} = \Delta\epsilon(e_\uparrow^{1.5}e_\downarrow^{0.5}). \tag{8}$$

The reduction of the electron repulsion in solids compared to isolated ions has been called the nephelauxetic effect. In the DVME method, the covalency which is expressed by the mixing of atomic orbitals, and the correlation-correction factor C are the factors used to reduce the electron repulsion.

To obtain a theoretical absorption spectrum, the oscillator strength of the electric dipole transition I_{fi} is calculated from

$$I_{fi} = 2(E_f - E_i)\left|\int \cdots \int \Psi_f^* \sum_{j=1}^{N} \boldsymbol{r}_j \cdot \frac{\boldsymbol{E}}{|\boldsymbol{E}|} \Psi_i \, \mathrm{d}\boldsymbol{r}_1 \, \mathrm{d}\boldsymbol{r}_2 \cdots \mathrm{d}\boldsymbol{r}_N\right|^2 \tag{9}$$

where the subscripts i and f mean the initial and the final states, respectively, E_i and E_f are their energies, and $\boldsymbol{E}$ is the electric field of the incident light. A theoretical spectrum is obtained by applying the oscillator strength to the Lorentz resonance curve with a full width at half-maximum of $325\ cm^{-1}$. The theoretical spectra are shown just to make it easy to compare the calculated results with the experimentally obtained absorption spectrum.

2.2. Cluster models

The data on the crystal structures of Mg_2SiO_4 (forsterite) [13], $Ca_2MgSi_2O_7$ (åkermanite) [14], and Y_2SiO_5 (YSO) [15] host crystals are summarized in table 1. Since the three crystals belong to different crystal systems, each anisotropy produces the corresponding polarization dependence of the absorption spectra. All of the crystals possess distorted SiO_4 coordination tetrahedra, whose Si–O bond lengths differ from each other. The symmetries at the Si sites are C_s in forsterite and åkermanite, and C_1 in YSO, reduced from T_d symmetry. In all of the crystals, the prominent structures of the absorption spectra have been supposed to originate from the tetrahedrally coordinated Cr^{4+} that replaced the Si atom, although in forsterite, for example, octahedrally coordinated Cr^{3+} coexists with it [16].

Table 1. The crystal structures of forsterite, åkermanite, and YSO.

	Forsterite (Mg_2SiO_4)	Åkermanite ($Ca_2MgSi_2O_7$)	YSO (Y_2SiO_5)
Crystal system	Orthorhombic, $Pbnm$	Tetragonal, $P\bar{4}2_1m$	Monoclinic, $C2/c$
a (Å)	4.756	7.8335	10.410
b (Å)	10.207		6.721
c (Å)	5.980	5.0025	12.490
β (deg)	90	90	102.39
Symmetry at Si site	C_s	C_s	C_1
Si–O(1) (Å)	1.615	1.597	1.623
Si–O(2) (Å)	1.635	1.623	1.633
Si–O(3) (Å)	1.653	1.658	1.629
Si–O(4) (Å)			1.655

In this paper, we concentrate on the electronic structures of the tetrahedrally coordinated Cr^{4+} in forsterite, åkermanite, and YSO crystals. The geometries of the cluster models for the three crystals are drawn in figures 1, 2, and 3. For each crystal, we used three cluster models, A, B, and C, to examine the dependence of the size of the models on the calculated
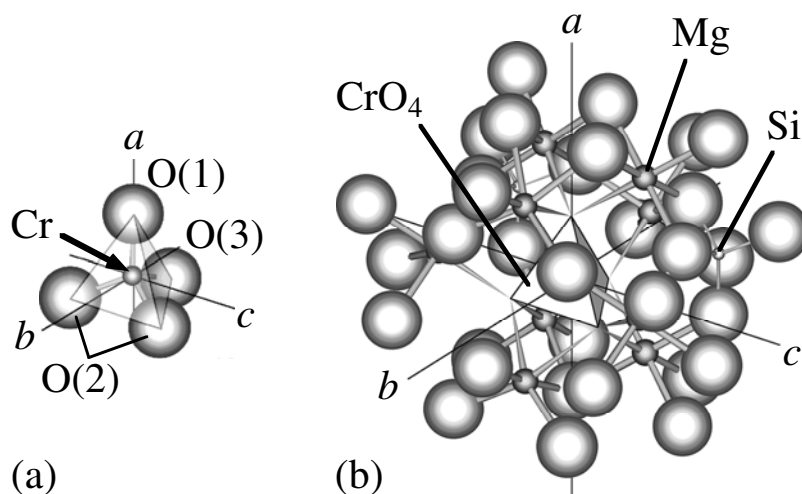
Figure 1. The geometry of the cluster models for Cr^{4+}:forsterite. (a) $(CrO_4)^{4-}$ models A and B, and (b) $(CrMg_9Si_2O_{37})^{44-}$ model C. In models B and C, additional point charges with formal valences are placed at the atomic sites outside the clusters to reproduce the effective Madelung potential. The symmetry at the centre Cr atoms is C_s.

Figure 2. The geometry of the cluster models for Cr^{4+}:åkermanite. (a) $(CrO_4)^{4-}$ models A and B, and (b) $(CrCa_6Mg_2SiO_{38})^{52-}$ model C. In models B and C, additional point charges with formal valences are placed at the atomic sites outside the clusters to reproduce the effective Madelung potential. The symmetry at the centre Cr atoms is C_s.

multiplet structures. The $(CrO_4)^{4-}$ models A were simply cut out from the crystal structures, centred at the Si atom, which was substituted for with a Cr atom. The difference in the crystal structures is expressed only by the different Cr–O bond lengths and ∠O–Cr–O bond angles. The four O atoms in the forsterite and åkermanite models were classified into three sites; on the other hand, all four O atoms were different in YSO. The numbers labelling each O atom in figures 1, 2, and 3 correspond to those in table 1. The $(CrO_4)^{4-}$ models B

Figure 3. The geometry of the cluster models for Cr^{4+}:YSO. (a) $(CrO_4)^{4-}$ models A and B, and (b) $(CrY_8O_{37})^{46-}$ model C. In models B and C, additional point charges with formal valences are placed at the atomic sites outside the clusters to reproduce the effective Madelung potential. The symmetry at the centre Cr atoms is C_1.
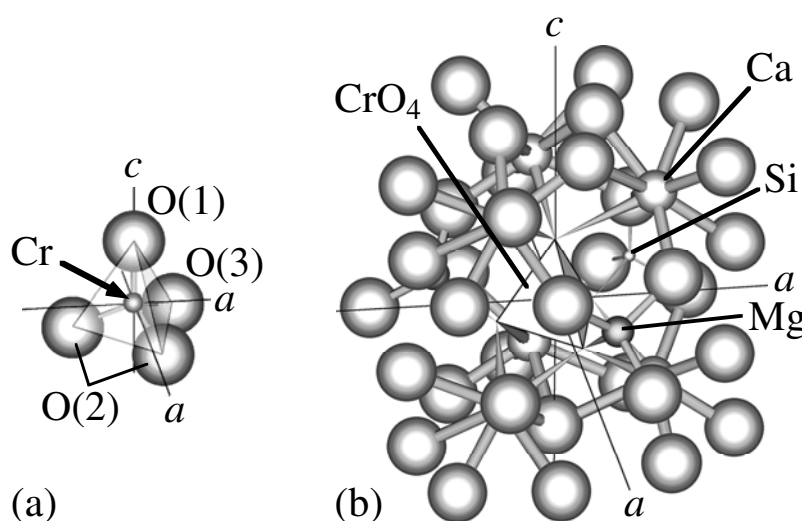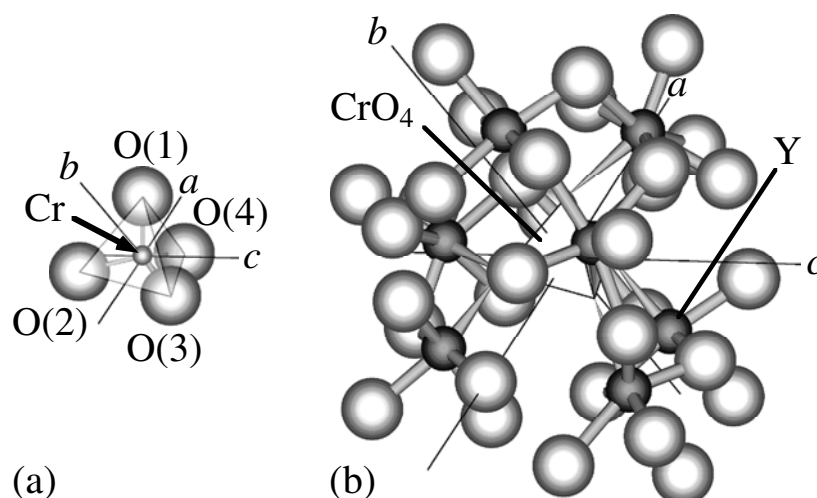
possessed the same atoms as models A, and were extended to reproduce the effective Madelung potentials, by placing additional point charges with formal valences at the atomic sites outside the five atoms within the spatial region of $6 \times 6 \times 6$ unit cells. The Mg, Si, Ca, Y, and O atoms outside the CrO_4 tetrahedron were approximated by +2, +4, +2, +3, and −2 point charges, respectively. The size of models A and B with five atoms corresponds to the size of the models that have been considered in the traditional ligand-field theory. The models C, $(CrMg_9Si_2O_{37})^{44-}$ for forsterite, $(CrCa_6Mg_2SiO_{38})^{52-}$ for åkermanite, and $(CrY_8O_{37})^{46-}$ for YSO, were further extended from the models B by adding atoms around the CrO_4 tetrahedra. The four O atoms around the Cr atom (ligand O atoms) were completely shared by the first-shell-cation coordination polyhedra. In the forsterite model, the two Si atoms did not directly share the ligand O atoms.

3. Results and discussion

3.1. One-electron MO calculation

3.1.1. One-electron MO energies. The calculated one-electron MO energies obtained from the forsterite, åkermanite, and YSO models are shown in figures 4, 5, and 6, respectively. The results (a), (b), and (c) correspond to the results obtained from models A, B, and C, respectively. The lowest Cr 3d levels, which two electrons occupied, were set at zero. The MOs of the valence band were composed of the O 2p orbitals. The MOs of the unoccupied levels (conduction bands) were only composed of the Cr 4s and Cr 4p orbitals in the results obtained from the small models A and B; on the other hand, they were mainly composed of the other cations' orbitals in the results obtained from the larger models C. The impurity levels whose MOs were mainly composed of the Cr 3d orbitals were located between the O 2p valence band and the conduction bands. The impurity levels in the calculated results completely split into five levels due to the ligand field with low symmetries. Nevertheless, we see that the T_d-symmetry-like energy structure was still preserved—that is, the lower two MOs
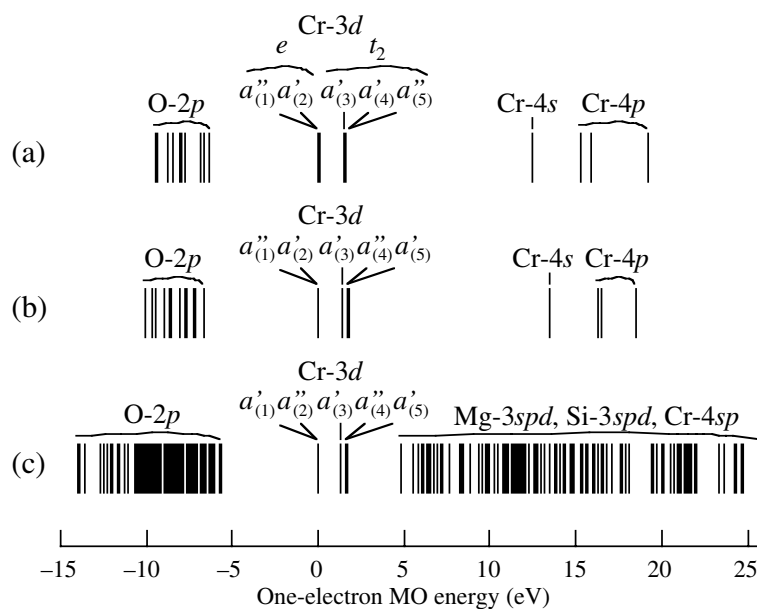
Figure 4. The calculated one-electron MO energies obtained from the forsterite models A, B, and C.

Figure 5. The calculated one-electron MO energies obtained from the åkermanite models A, B, and C.

originated from the twofold-degenerate e symmetry and the higher three MOs originated from the threefold-degenerate t_2 symmetry. We use this expression in the T_d symmetry to clearly specify the electron configuration. The five impurity-level MOs were taken to construct the Slater determinants in equation (2).
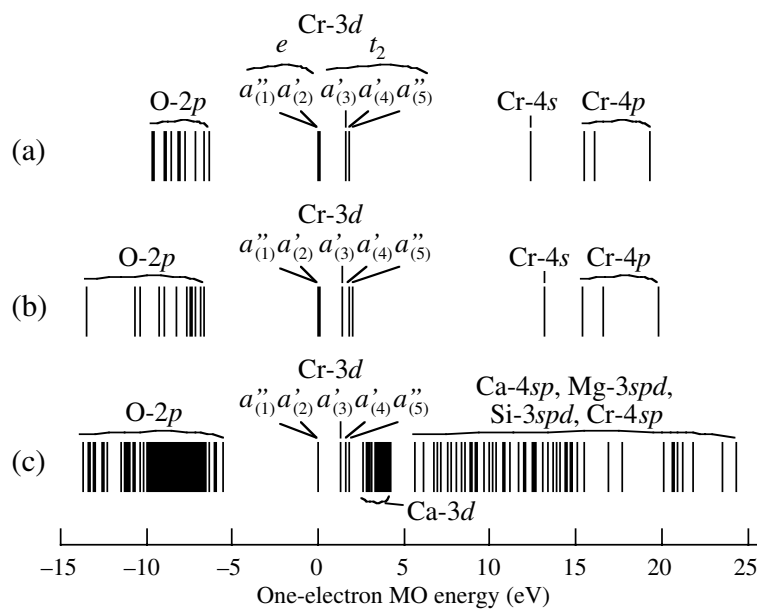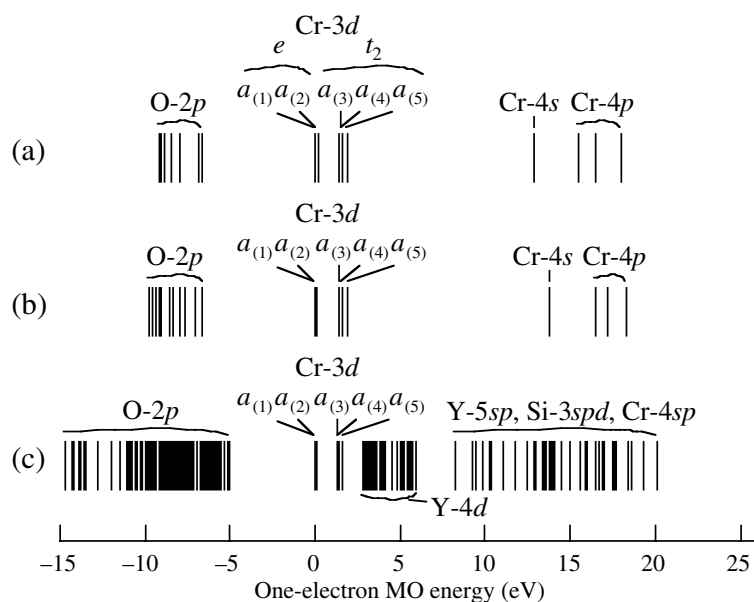
Figure 6. The calculated one-electron MO energies obtained from the YSO models A, B, and C.

In the results obtained from the forsterite models with C_s symmetry in figure 4, the five impurity-level MOs had either a' or a'' symmetry (lower-case letters are used for one-electron calculations). We attached the labels (1)–(5) to those MOs in the order of their energies. Comparing the results in figure 4 with each other, we see that the order of the impurity-level MOs changed according to the models. The order of the energies of the $a'_{(4)}$ and $a''_{(5)}$ states in model A was reversed in model B. The order of the energies of the $a''_{(1)}$ and $a'_{(2)}$ states is further reversed as we go on to the result obtained from model C. As for the dependence of the magnitude of the energy splittings on the models, we find that the dependence of the energy splitting between the a' and a'' states originating from the e symmetry was negligibly small ($\leqslant 0.03$ eV); on the other hand, the dependence of the energy splitting of the states originating from the t_2 symmetry was large ($\geqslant 0.27$ eV). As a result, the overall structures of the impurity levels obtained from models B and C were similar, but did not resemble that obtained from model A. In the result obtained from model C, the conduction band was mainly composed of Mg 3s, Mg 3p, Mg 3d, Si 3s, Si 3p, and Si 3d orbitals. In this case, the impurity-level MOs are expected to be composed not only of the O 2p orbitals but also of those cations' orbitals.

In the results obtained from the åkermanite models with C_s symmetry in figure 5, the order of the MOs according to their energies was $a''_{(1)}$, $a'_{(2)}$, $a'_{(3)}$, $a'_{(4)}$, and $a''_{(5)}$, independently of the model. The energy splitting between the $a'_{(3)}$ and $a'_{(4)}$ states was small, 0.03 eV, in model A, but large, 0.45 eV and 0.31 eV, respectively, in models B and C. Here again, the overall energy structures of the impurity levels obtained from models B and C showed a resemblance, but were different from that obtained from model A. The O 2p valence band obtained from model B had a larger bandwidth compared to that obtained from model A. This indicates that the effective Madelung potential in model B further enhanced the difference between the potentials on the O atoms. In the result obtained from model C, the conduction band was mainly composed of Ca 3d, Ca 4s, Ca 4p, Mg 3s, Mg 3p, Mg 3d, Si 3s, Si 3p, and Si 3d orbitals. The lowest-energy region was dominated by the Ca 3d orbitals, which are expected to affect the multiplet structure.

The calculated results obtained from the YSO models are shown in figure 6. Since the symmetry at the Cr site was the lowest, C_1, the impurity levels had only the symmetry a, and the MOs are denoted as $a_{(1)}$, $a_{(2)}$, $a_{(3)}$, $a_{(4)}$, $a_{(5)}$ in order of their energies. In this case, all of the impurity levels showed similar energy splittings in the three models. In the result obtained from model C, the conduction band was mainly composed of Y 4d, Y 5s, Y 5p, Si 3s, Si 3p, and Si 3d orbitals. The lowest region was mainly composed of the Y 4d orbitals, which are expected to join the impurity-level MOs.

3.1.2. The covalency of impurity-level MOs. Covalency is an important factor when we analyse the multiplet structure that was produced by impurity centres. The covalency of impurity-level MOs was evaluated by the population-analysis method proposed by Mulliken [17]. The contribution of atomic orbitals to the MOs was numerically analysed by summarizing the coefficients c_{pq} in equation (1), and the results are shown in tables 2, 3, and 4, for the forsterite, åkermanite, and YSO models, respectively. The results were classified into the contributions of Cr 3d, Cr (4s + 4p), ligand O 2s, O 2p, and of all the other cations' orbitals making up the conduction bands (except the Y 4p orbitals). The results for the ligand O 2p orbitals were further classified into the contributions of the three (forsterite and åkermanite) or the four (YSO) different O atoms. The contributions of the first-shell-cation orbitals obtained from the larger models C were summarized from all of the atoms making up the clusters, but the contributions of the O atoms outside the CrO_4 tetrahedra are not shown in the tables.

Table 2. The result of Mulliken population analyses obtained from the forsterite models.

Model	MO	Cr		Ligand O					Mg	Si
		3d	4s + 4p	2s	2p				3s + 3p + 3d	3s + 3p + 3d
					O(1)	O(2)	O(3)	Total		
A	$a''_{(1)}$(e)	0.85	0.00	0.00	0.02	0.08	0.05	0.15		
	$a'_{(2)}$(e)	0.85	0.00	0.00	0.03	0.09	0.04	0.15		
	$a'_{(3)}$(t_2)	0.72	0.07	0.01	0.08	0.07	0.06	0.20		
	$a'_{(4)}$(t_2)	0.70	0.08	0.01	0.04	0.09	0.08	0.21		
	$a''_{(5)}$(t_2)	0.70	0.08	0.01	0.04	0.16	0.02	0.21		
B	$a''_{(1)}$(e)	0.86	0.00	0.00	0.03	0.07	0.04	0.14		
	$a'_{(2)}$(e)	0.86	0.00	0.00	0.04	0.08	0.02	0.14		
	$a'_{(3)}$(t_2)	0.72	0.06	0.01	0.10	0.09	0.02	0.21		
	$a''_{(4)}$(t_2)	0.71	0.07	0.01	0.04	0.16	0.01	0.21		
	$a'_{(5)}$(t_2)	0.73	0.06	0.01	0.03	0.08	0.10	0.20		
C	$a'_{(1)}$(e)	0.82	0.00	0.00	0.03	0.08	0.03	0.14	0.04	0.00
	$a''_{(2)}$(e)	0.82	0.00	0.00	0.02	0.08	0.05	0.15	0.03	0.00
	$a'_{(3)}$(t_2)	0.67	0.06	0.01	0.08	0.08	0.03	0.19	0.07	0.00
	$a''_{(4)}$(t_2)	0.67	0.07	0.01	0.03	0.15	0.01	0.19	0.05	0.00
	$a'_{(5)}$(t_2)	0.69	0.06	0.01	0.02	0.08	0.09	0.20	0.04	0.00

From the results, we see that the primary component of the impurity-level MOs was the Cr 3d orbitals, and the O 2p orbitals mixed with them. Usually, the electron configuration of a Cr^{4+} ion is simply denoted as d^2 in atomic notation. However, the results mean that the electron configuration is better written explicitly as CrO_4^{4-}. The decrease of the proportions of

Table 3. The result of Mulliken population analyses obtained from the åkermanite models.

Model	MO	Cr 3d	Cr 4s + 4p	Ligand O 2s	Ligand O 2p O(1)	Ligand O 2p O(2)	Ligand O 2p O(3)	Ligand O 2p Total	Ca 3d + 4s + 4p	Mg 3s + 3p + 3d	Si 3s + 3p + 3d
A	$a''_{(1)}$(e)	0.85	0.00	0.00	0.05	0.02	0.08	0.15			
	$a'_{(2)}$(e)	0.85	0.00	0.00	0.04	0.03	0.08	0.15			
	$a'_{(3)}$(t_2)	0.68	0.10	0.01	0.12	0.04	0.06	0.21			
	$a'_{(4)}$(t_2)	0.73	0.06	0.01	0.03	0.07	0.10	0.20			
	$a''_{(5)}$(t_2)	0.70	0.08	0.01	0.01	0.04	0.16	0.21			
B	$a''_{(1)}$(e)	0.85	0.00	0.00	0.02	0.03	0.10	0.15			
	$a'_{(2)}$(e)	0.85	0.00	0.00	0.02	0.05	0.08	0.15			
	$a'_{(3)}$(t_2)	0.74	0.08	0.02	0.05	0.05	0.07	0.17			
	$a'_{(4)}$(t_2)	0.70	0.07	0.00	0.01	0.10	0.11	0.22			
	$a''_{(5)}$(t_2)	0.69	0.08	0.01	0.00	0.06	0.16	0.23			
C	$a''_{(1)}$(e)	0.82	0.00	0.00	0.03	0.08	0.03	0.14	0.02	0.01	0.01
	$a'_{(2)}$(e)	0.81	0.00	0.00	0.04	0.08	0.02	0.14	0.03	0.01	0.01
	$a'_{(3)}$(t_2)	0.65	0.08	0.02	0.04	0.07	0.06	0.16	0.06	0.01	0.02
	$a'_{(4)}$(t_2)	0.62	0.07	0.00	0.09	0.09	0.02	0.19	0.09	0.01	0.01
	$a''_{(5)}$(t_2)	0.63	0.08	0.01	0.06	0.14	0.01	0.20	0.05	0.03	0.00

the contribution of the Cr 3d orbitals can be regarded as a degree of covalency. We see from the results that the contribution of the Cr 3d orbitals to the MOs originating from e symmetry was 0.11–0.23 larger than the contribution to the MOs originating from t_2 symmetry. This difference generally forced the traditional semiempirical methods to introduce an additional adjustable parameter.

In the case of Cr^{4+} in $Y_3Al_5O_{12}$ (YAG), we had obtained the contributions of the Cr 3d orbitals, 0.80–0.87 for e symmetry and 0.70–0.76 for t_2 symmetry, and the difference between the e and t_2 symmetries was 0.07–0.13 [18]. Comparing with the results on Cr^{4+}:YAG, we found that the contribution of the Cr 3d orbitals in the three silicate crystals in this study lay in the same range for MOs originating from e symmetry, but was smaller by 0.04 on average for t_2 symmetry. This smaller value is ascribed to the neglect of the lattice relaxation around the Cr^{4+} ion that was substituted for the Si^{4+} ion with a smaller ionic radius. In the case of Cr^{4+}:YAG, the relaxation could fortunately be considered negligible because the substituted Al^{3+} ion had almost the same ionic radius as the Cr^{4+} ion. We should note that the covalency was a little overestimated in this study, since the bond lengths in the cluster models were smaller than they should be. As a result, the calculated positions of the impurity levels in the band gap, shown in figures 4–6, would be highly overestimated. Nevertheless, we consider that the overestimation of the covalency is less important than the apparent differences between the absorption spectra, such as the polarization dependence produced by the different crystals.

Comparing the results obtained from the forsterite and åkermanite models A in tables 2 and 3, we find that the tendencies of the contributions of the 2p orbitals of the O(1), O(2), and O(3) atoms were not the same. This might seem strange, because the Cr–O bond lengths increased in the same order, O(1) < O(2) < O(3). Also the differences in bond angles have affected the covalency. We consider such a difference in the covalency to be important.

Table 4. The result of Mulliken population analyses obtained from the YSO models.

| Model | MO | Cr | | Ligand O | | | | | | | Y | |
		3d	4s + 4p	2s	O(1)	O(2)	O(3)	O(4)	Total	4d	4p + 5s + 5p
A	$a_{(1)}(e)$	0.85	0.00	0.00	0.04	0.04	0.03	0.04	0.15		
	$a_{(2)}(e)$	0.85	0.00	0.00	0.04	0.05	0.03	0.03	0.15		
	$a_{(3)}(t_2)$	0.72	0.06	0.01	0.05	0.05	0.05	0.06	0.21		
	$a_{(4)}(t_2)$	0.72	0.07	0.01	0.05	0.04	0.06	0.06	0.21		
	$a_{(5)}(t_2)$	0.70	0.08	0.01	0.07	0.06	0.05	0.04	0.21		
B	$a_{(1)}(e)$	0.86	0.00	0.00	0.03	0.04	0.03	0.04	0.14		
	$a_{(2)}(e)$	0.86	0.00	0.00	0.03	0.04	0.04	0.03	0.14		
	$a_{(3)}(t_2)$	0.74	0.06	0.01	0.04	0.06	0.05	0.05	0.19		
	$a_{(4)}(t_2)$	0.73	0.06	0.01	0.04	0.05	0.06	0.06	0.20		
	$a_{(5)}(t_2)$	0.72	0.07	0.01	0.06	0.07	0.04	0.04	0.20		
C	$a_{(1)}(e)$	0.81	0.00	0.00	0.03	0.04	0.03	0.04	0.13	0.05	0.01
	$a_{(2)}(e)$	0.80	0.00	0.00	0.03	0.04	0.04	0.03	0.14	0.05	0.01
	$a_{(3)}(t_2)$	0.64	0.05	0.01	0.03	0.05	0.05	0.03	0.16	0.12	0.01
	$a_{(4)}(t_2)$	0.63	0.06	0.01	0.04	0.03	0.04	0.06	0.16	0.14	0.01
	$a_{(5)}(t_2)$	0.58	0.06	0.01	0.03	0.06	0.02	0.03	0.14	0.19	0.01

When point charges were placed outside the clusters, the covalency changed. The largest change was observed in the åkermanite model B, shown in table 3. The contribution of the O 2p orbitals to $a'_{(3)}(t_2)$ was reduced compared to that obtained from model A. This is related to the fact that the width of the O 2p valence band in figure 3(b) was wider than the band in figure 3(a). In all of the crystals, the Cr atoms in models B showed stronger ionic character than those in models A, since the ligand O 2p orbitals were primarily attracted by the first-nearest-cation point charges, and the Cr–O interactions were reduced. In the results of models C, we see that the first-shell-cation orbitals also contributed to the impurity-level MOs, and further reduced the contribution of the Cr 3d orbitals. These changes in the covalency are expected to affect the polarization dependence of the calculated absorption spectra. In every crystal, the magnitude of the contribution of the Cr 3d orbitals tended to decrease in the following order of models: B > A > C.

In the forsterite model C, the Mg 3s, Mg 3p, and Mg 3d orbitals further reduced the contribution of the Cr 3d orbitals; on the other hand, the Si 3s, Si 3p, and Si 3d orbitals made only negligible contributions to the impurity-level MOs. This is because the SiO$_4$ coordination tetrahedra did not directly make contact with the CrO$_4$ tetrahedron, whereas the Mg atoms shared the ligand O atoms with the Cr atom. From this result, we conclude that the wave functions of the impurity levels spread beyond the ligand O atoms, and the furthest effective spatial region was the first-shell-cation coordination polyhedra. The same conclusion had been derived also from the calculations on Cr^{4+}:YAG [18]. In the result obtained from the YSO model C in table 4, a large contribution of the Y 4d orbitals to the impurity-level MOs originating from the t$_2$ symmetry was observed. The contribution was an order of magnitude larger than that obtained from the calculations on Cr^{4+}:YAG, which also contained Y atoms. We consider that the calculated contribution of the Y 4d orbitals in the YSO was rather overestimated, and this is ascribable to the neglect of the lattice relaxation around the Cr

atom. Since the energy positions of the impurity levels were highly overestimated, the levels came closer to the Y 4d levels, which produced a strong interaction with the Cr 3d orbitals. Since the accuracy requirement in the geometry optimization for the multiplet calculation, which is not a general one-electron calculation, is severe for any computational code, we left the problem of the lattice relaxation untouched in this study.

3.2. Multiplet structure calculation

3.2.1. The CDC and CIC approaches. In this subsection, we discuss the technical aspects of the method. We compare the results obtained by the CDC and the CIC approaches. We show here that the essence of the discussion in the next subsection based on the CIC approach with a scaling factor is the same as for the CDC approach without such a factor. The calculated multiplet energies and the transition probabilities (theoretical absorption spectra) obtained from the forsterite models C by the CDC and the CIC approaches are shown in figures 7(a) and 7(b), respectively. The calculated multiplet energies are shown as straight lines, classified into the singlet states (upper) and the triplet states (lower). The ground state was set at zero. The states were taken up to $35\,000$ cm^{-1}. The multiplet-term symbols within a parent T_d symmetry were attached to the states. The triplet terms included the $^3A_2$ term in the ground-state electron configuration (e^2), the $^3T_2$ and $^3T_1$ terms in the one-electron-excitation electron configuration (et_2), and another $^3T_1$ term in the two-electron-excitation electron configuration (t_2^2). For the triplet terms, the symmetries of the states in the exact C_s symmetry, A' and A'', were also attached. The ground state was $^3A''$, and we
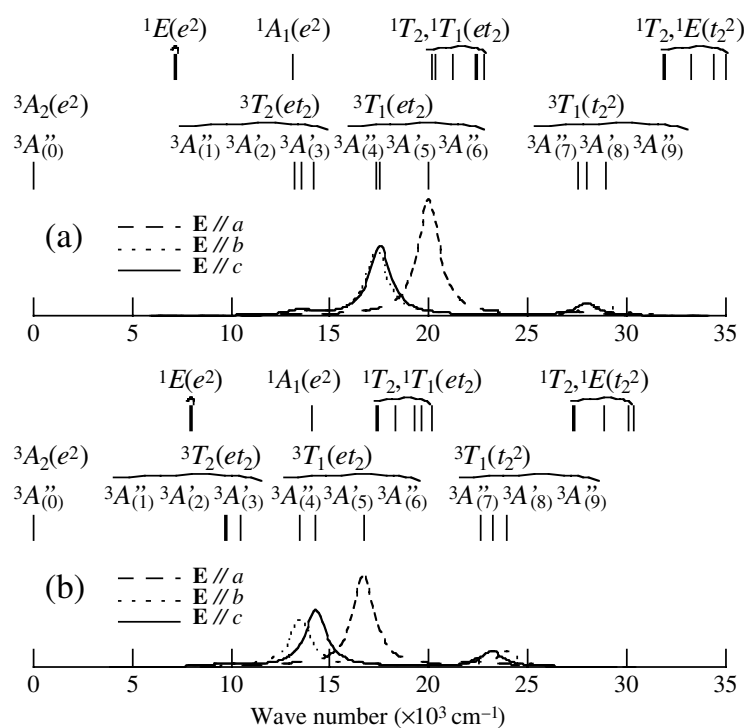

Figure 7. The calculated multiplet energies (upper) and the theoretical absorption spectra (below), obtained from the forsterite models C, (a) by the CDC approach, and (b) by the CIC approach.

denoted it as $^3A''_{(0)}[^3A_2(e^2)]$ to show the origin in the parent T_d symmetry and the electron configuration. The nine excited triplet states were numbered in order of their energies, and were denoted as $^3A''_{(1)}[^3T_2(et_2)]$, $^3A'_{(2)}[^3T_2(et_2)]$, $^3A'_{(3)}[^3T_2(et_2)]$, $^3A''_{(4)}[^3T_1(et_2)]$, $^3A'_{(5)}[^3T_1(et_2)]$, $^3A''_{(6)}[^3T_1(et_2)]$, $^3A''_{(7)}[^3T_1(t_2^2)]$, $^3A'_{(8)}[^3T_1(t_2^2)]$, and $^3A''_{(9)}[^3T_1(t_2^2)]$. For the lowest field in figures 7(a) and 7(b), the theoretical absorption spectra are depicted. The theoretical spectra were obtained from equation (9), where the initial state was the ground state, and the final state was all the excited triplet states. The relative height of the spectra was preserved throughout the figures, and can be compared between them. The theoretical spectra showed polarization dependence, which is indicated by the different types of line. As an example, $E \parallel a$ polarization means that the electric vector of the incident light is parallel to the crystallographic a-axis.

The substantial difference between the results obtained by the CDC and the CIC approaches lay in the mean energy of each multiplet term. In the CDC approach, the calculated effective ligand-field splitting, expressed by equation (5), was estimated to be larger than it should be, due to the neglect of the lattice relaxation. On the other hand, in the CIC approach, we selected the scaling factor to reproduce the peak positions in the experimentally obtained absorption spectrum (see figure 8(d)). So the energy difference between the mean energies of the electron configurations, corresponding to the effective ligand-field splitting, was smaller than that obtained by the CDC approach. As a result, the triplet states in the CIC approach shifted toward lower energy. Still we see that the orders of the calculated symmetries of the states, according to the energies, were the same as derived in the two approaches. This means that the overall energy structures were qualitatively independent of the approaches applied. Furthermore, the intensity ratio and the polarization dependence did not show any significant changes between the two results. As long as we are discussing the relative positions of states, the transition probability, and the polarization dependence, and not the absolute value of the energy, the CDC and CIC approaches lead to the same conclusions in practice. In this study, as we fixed the scaling factor at a constant, the discussion on the differences in the spectra among the three crystals is not affected by the factor. Although we could base the subsequent discussion on the results obtained by the *ab initio* CDC approach, we used the results obtained by the CIC approach, to show the correspondence with the experimentally obtained spectra also as regards the calculated energies. Hereafter, all discussion is based on the results obtained by the CIC approach.

3.2.2.   The multiplet energies and the transition probabilities of the silicate crystals. The calculated multiplet energies and the theoretical spectra obtained from the forsterite, åkermanite, and YSO models are shown in figures 8, 9, and 10, respectively. Parts (a), (b), and (c) corresponded to the results obtained from models A, B, and C, respectively. Parts (d) are the experimentally obtained absorption spectra taken from references [19–21], for comparison. The calculated oscillator strengths of the transitions to the triplet states obtained from the forsterite, åkermanite, and YSO models C are listed in tables 5, 6, and 7, respectively. In the experimentally obtained spectrum of Cr^{4+}:YSO in figure 10(d), only the $E \parallel b$ polarization has definitely been determined, as far as we know, in the literature. So the intensity ratios for the other polarizations are actually uncertain, and we left the indications of the polarizations as they were. However, we consider that the $E \parallel n_1$ polarization was $E \parallel c$-like polarization, from comparing the spectrum with the similar spectrum obtained by Koetke *et al* [22], who determined only the c-axis. Thus we consider that the $E \parallel n_1$ and $E \parallel n_3$ polarizations were $E \parallel c$-like and $E \parallel a$-like polarizations, respectively. In all of the spectra, we have shown the details in the insets, where the range of the intensity was chosen arbitrarily for each one.

Figure 8. (a)–(c) The calculated multiplet energies (upper) and the theoretical absorption spectra (below and in insets) obtained from the forsterite models A, B, and C. (d) The experimentally obtained absorption spectrum taken from reference [19].

Figure 9. (a)–(c) The calculated multiplet energies (upper) and the theoretical absorption spectra (below and in insets) obtained from the åkermanite models A, B, and C. (d) The experimentally obtained absorption spectrum taken from reference [20].
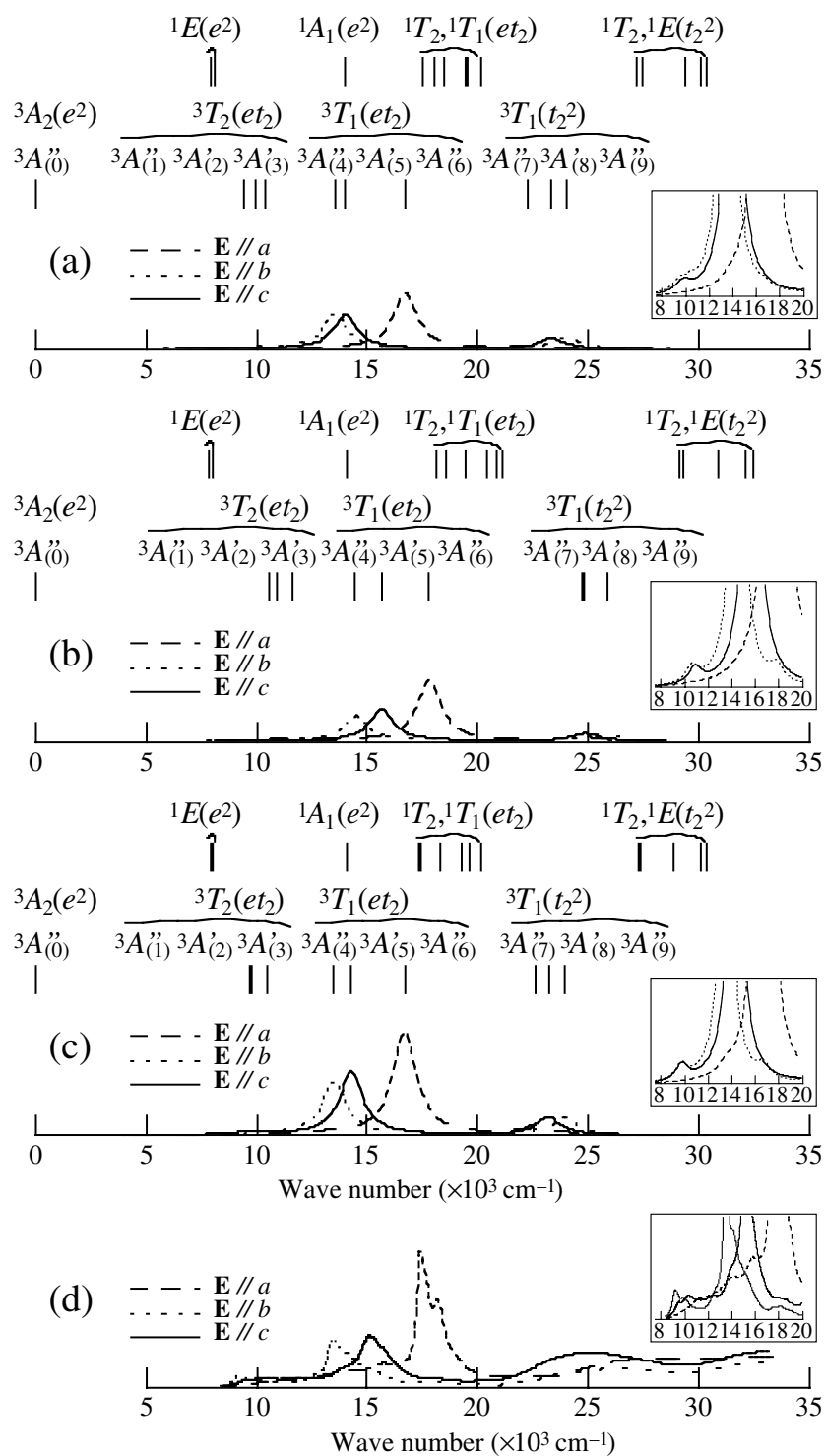
Figure 10. (a)–(c) The calculated multiplet energies (upper) and the theoretical absorption spectra (below and in insets) obtained from the YSO models A, B, and C. (d) The experiment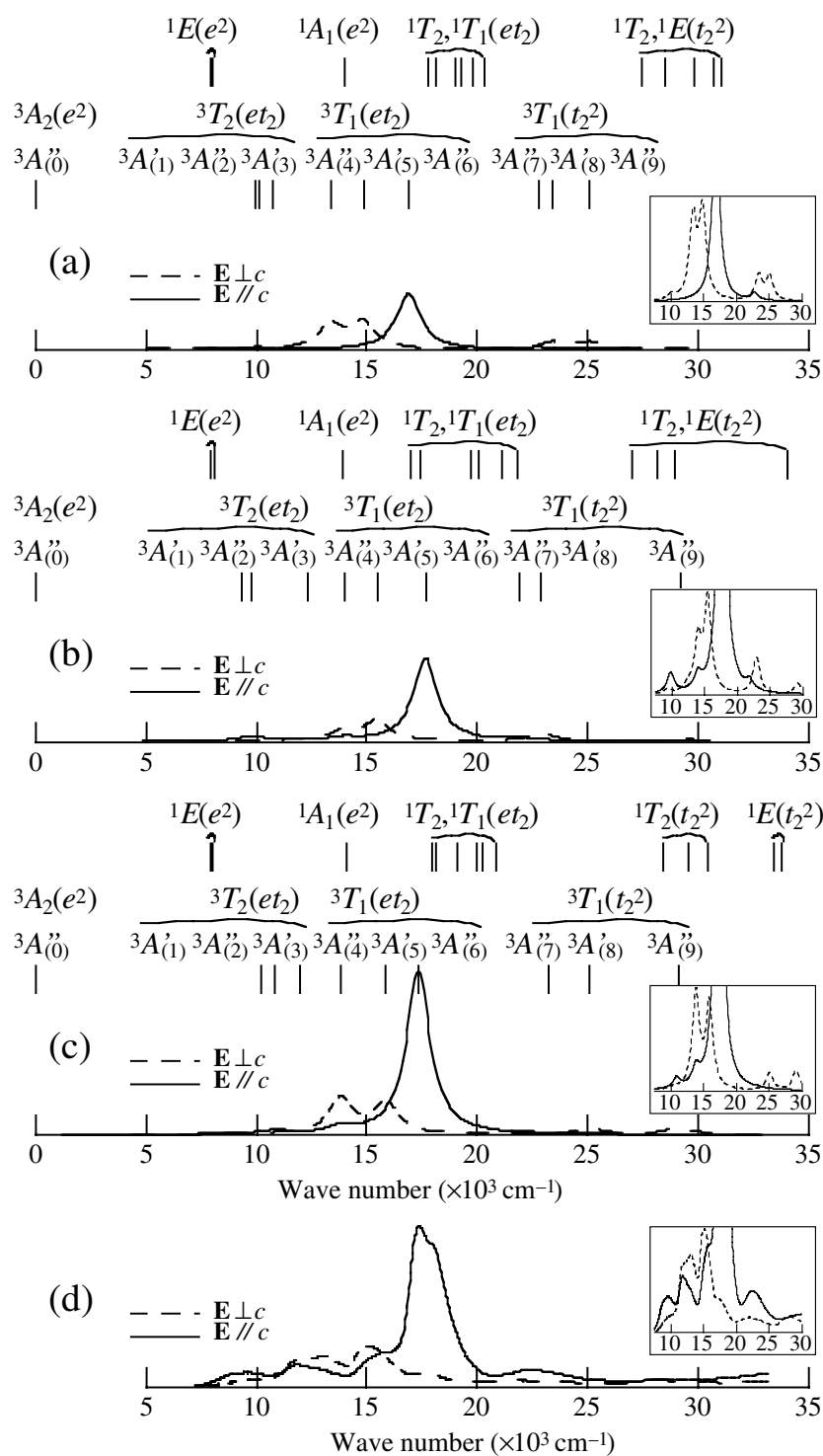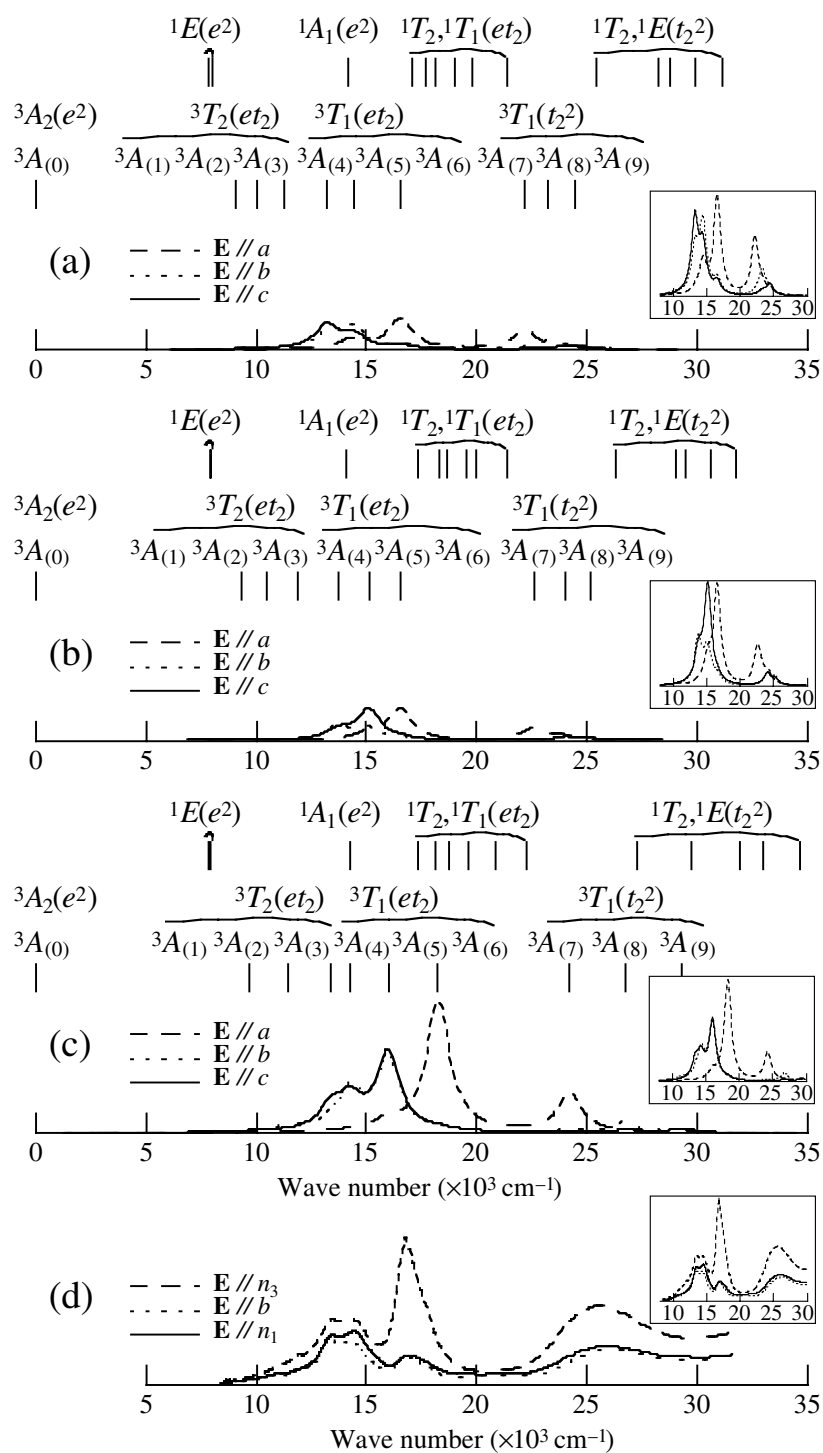ally obtained absorption spectrum taken from reference [21]. The $E \parallel n_3$ and $E \parallel n_1$ polarizations were not clearly defined in the literature.

Table 5. The calculated oscillator strengths of spin-allowed transitions, obtained from the forsterite model C.

State	$E \parallel a$	$E \parallel b$	$E \parallel c$
$^3A''_{(1)}[^3T_2(et_2)]$	0	5.1×10^{-4}	
$^3A'_{(2)}[^3T_2(et_2)]$			5.5×10^{-4}
$^3A'_{(3)}[^3T_2(et_2)]$			0
$^3A''_{(4)}[^3T_1(et_2)]$	3.1×10^{-4}	1.1×10^{-2}	
$^3A'_{(5)}[^3T_1(et_2)]$			1.3×10^{-2}
$^3A''_{(6)}[^3T_1(et_2)]$	2.1×10^{-2}	4.8×10^{-4}	
$^3A''_{(7)}[^3T_1(t_2^2)]$	1.8×10^{-3}	2.7×10^{-4}	
$^3A'_{(8)}[^3T_1(t_2^2)]$			3.5×10^{-3}
$^3A''_{(9)}[^3T_1(t_2^2)]$	9.4×10^{-5}	3.3×10^{-3}	

Table 6. The calculated oscillator strengths of spin-allowed transitions, obtained from the åkermanite model C.

State	$E \perp c$	$E \parallel c$
$^3A'_{(1)}[^3T_2(et_2)]$		2.0×10^{-4}
$^3A''_{(2)}[^3T_2(et_2)]$	5.9×10^{-4}	
$^3A'_{(3)}[^3T_2(et_2)]$		3.1×10^{-5}
$^3A''_{(4)}[^3T_1(et_2)]$	8.4×10^{-3}	
$^3A'_{(5)}[^3T_1(et_2)]$		9.4×10^{-3}
$^3A''_{(6)}[^3T_1(et_2)]$	3.3×10^{-2}	
$^3A''_{(7)}[^3T_1(t_2^2)]$	5.1×10^{-5}	
$^3A'_{(8)}[^3T_1(t_2^2)]$		1.9×10^{-3}
$^3A''_{(9)}[^3T_1(t_2^2)]$	1.6×10^{-3}	

Table 7. The calculated oscillator strengths of spin-allowed transitions, obtained from the YSO model C.

State	$E \parallel a$	$E \parallel b$	$E \parallel c$
$^3A_{(1)}[^3T_2(et_2)]$	0	1.3×10^{-4}	1.3×10^{-4}
$^3A_{(2)}[^3T_2(et_2)]$	1.3×10^{-4}	9.5×10^{-4}	0
$^3A_{(3)}[^3T_2(et_2)]$	1.3×10^{-5}	1.3×10^{-3}	4.6×10^{-3}
$^3A_{(4)}[^3T_1(et_2)]$	4.3×10^{-5}	7.8×10^{-3}	5.8×10^{-3}
$^3A_{(5)}[^3T_1(et_2)]$	2.2×10^{-3}	1.5×10^{-2}	1.6×10^{-2}
$^3A_{(6)}[^3T_1(et_2)]$	2.7×10^{-2}	3.0×10^{-4}	4.4×10^{-4}
$^3A_{(7)}[^3T_1(t_2^2)]$	7.8×10^{-3}	4.6×10^{-4}	5.7×10^{-5}
$^3A_{(8)}[^3T_1(t_2^2)]$	1.8×10^{-4}	2.2×10^{-3}	5.4×10^{-4}
$^3A_{(9)}[^3T_1(t_2^2)]$	3.7×10^{-4}	4.1×10^{-4}	7.5×10^{-4}

First, we see that the overall structures of the experimentally obtained spectra were reproduced by the theoretical ones. The strong peaks in the visible region originated from the transitions to the states in the $^3T_1(et_2)$ triplet term; on the other hand, the weak NIR

peaks originated from the $^3T_2(et_2)$ triplet term. From these results, we can confirm that the apparent structures in the absorption spectra of the three Cr^{4+}-doped silicate crystals originated from the tetrahedrally coordinated Cr^{4+} state. The same structures were also obtained by the CDC approach, although the energies were overestimated. As a rough estimate from tables 5–7, the calculated magnitudes of the oscillator strengths of the transitions were about 1×10^{-4} for $^3T_2(et_2)$ in the NIR region, and about 1×10^{-2} for $^3T_1(et_2)$ in the visible region. For Cr^{4+}:Ca_2GeO_4, Hazenkamp *et al* experimentally deduced oscillator strengths of about 5×10^{-5} for $^3T_2(et_2)$, and about 9×10^{-4} for $^3T_1(et_2)$ [23]. We assume that the magnitudes of the oscillator strengths do not strongly depend on the crystals. We find that the calculated oscillator strengths are about an order of magnitude larger than those deduced experimentally. In the experimental analysis, the effective concentration of the tetrahedrally coordinated Cr^{4+} was unknown. We ascribe the inconsistency to the error in the effective concentration assumed by Hazenkamp *et al*. We consider that the effective concentration in their analysis should have been an order of magnitude smaller than they assumed.

Cr^{4+}:forsterite. The calculated multiplet energies in figure 8, obtained from the forsterite models, show the large energy splittings originating from the twofold-degenerate (E) and threefold-degenerate (T) parent multiplet terms. The overall structures of the triplet states showed a good agreement with the experimentally obtained spectrum. The calculated energies obtained from our three models and Hazenkamp's semiempirical AOM calculation [23] are listed in table 8, together with the experimentally obtained band maxima. We obtained the energy splittings without using any adjustable parameters for them, unlike Hazenkamp *et al*. In all of the results obtained from our models A, B, and C, the orders of the symmetries of the states according to the energies were the same. And the order corresponds to that obtained by the semiempirical AOM calculation. Thus we conclude that the spectral assignment for the triplet states obtained by Hazenkamp *et al* was likely to be correct. Since the order of the symmetries was unchanged among our three models, we consider that it is determined by the distortion of the CrO_4 tetrahedron from an exact tetrahedron, expressed by the smallest model A. However, as regards the energy splitting of the $^3T_1(et_2)$ triplet term, we find a better

Table 8. The calculated multiplet energies obtained from the forsterite models and Hazenkamp's semiempirical AOM calculation, and the experimentally obtained band maxima (in cm^{-1}).

State	Model A	Model B	Model C	AOM calculation[a]	Experiment[a]
$^3A''_{(1)}[^3T_2(et_2)]$	9426	10608	9702	9396	9150
$^3A'_{(2)}[^3T_2(et_2)]$	9927	10907	9772	9530	9820
$^3A'_{(3)}[^3T_2(et_2)]$	10351	11588	10504	10516	11500
$^3A''_{(4)}[^3T_1(et_2)]$	13525	14483	13507	13631	13600
$^3A'_{(5)}[^3T_1(et_2)]$	14015	15671	14280	14393	15100
$^3A''_{(6)}[^3T_1(et_2)]$	16733	17811	16700	17483	17460
$^3A''_{(7)}[^3T_1(t_2^2)]$	22241	24778	22650		
$^3A'_{(8)}[^3T_1(t_2^2)]$	23356	24874	23204	23786	22700
$^3A''_{(9)}[^3T_1(t_2^2)]$	24082	25855	23956		
$^1A''[^1E(e^2)]$	7902	7857	7919	8810	
$^1A'[^1E(e^2)]$	8087	8041	8028	8812	
$^1A'[^1A_1(e^2)]$	14014	14106	14057	14858	15240

[a] Reference [23].

agreement with the experimental result in the results obtained from models B and C than in those from model A. This is related to the fact that the impurity-level MOs of model A showed a different structure from those of models B and C.

As we directly constructed many-electron wave functions, we can also discuss the transition probability and its polarization dependence. The polarization dependence of the transitions from the $^3A''_{(0)}[^3A_2(e^2)]$ ground state to the three excited states in the $^3T_1(et_2)$ triplet term was consistent among the three models, and agreed with the polarization dependence of the experimentally obtained spectrum: $E \parallel b$, $E \parallel c$, and $E \parallel a$, in order of the energies. Also the polarization dependence of the $^3T_2(et_2)$ triplet term in the NIR region agreed with the experimentally obtained one. The spectra for the $E \parallel b$ and $E \parallel c$ polarizations possessed apparent peaks at about $10\,000$ cm^{-1}, whereas the spectrum for the $E \parallel a$ polarization had no peak, as shown in the insets. We confirmed that not only the peak energy but also the polarization dependence of the peak intensity were reproduced, without using any adjustable parameters to obtain them. As regards the states in the $^3T_1(t_2^2)$ triplet term, Hazenkamp *et al* mentioned two possibilities for the origin of the weak lines at about $18\,000$ cm^{-1} in the spectra for the $E \parallel b$ and $E \parallel c$ polarizations. They said that the lines could have originated from some $^3A''_{(0)}[^3A_2(e^2)] \rightarrow {}^1T_1(et_2)$ spin-forbidden transitions or from the $^3A''_{(0)}[^3A_2(e^2)] \rightarrow {}^3A''_{(7)}[^3T_1(t_2^2)]$ spin-allowed transition. We consider from our results that the possibility of the latter spin-allowed transition should be excluded, since the energy splitting of the $^3T_1(t_2^2)$ triplet term was not as large as that of the $^3T_1(et_2)$ term, and it is unlikely that the $^3A''_{(7)}[^3T_1(t_2^2)]$ state lay below $20\,000$ cm^{-1}. On the other hand, the energies of the states in the $^1T_2(et_2)$ and $^1T_1(et_2)$ singlet terms lay at around $18\,000$ cm^{-1}. As the many-electron wave functions of those states were composed of different Slater determinants with complex mixing, we could not classify any state either only into the $^1T_2(et_2)$ term or only into the $^1T_1(et_2)$ term. So we propose the possibility that Hazenkamp's weak lines at about $18\,000$ cm^{-1} originated from the transitions to the excited-singlet states originating from both the $^1T_2(et_2)$ and $^1T_1(et_2)$ singlet terms.

The calculated intensity ratio for the $^3T_1(et_2)$ triplet term got closer to the experimentally obtained one as the size of the models became larger. We consider that, besides showing the better agreement in the energy splitting, the largest model C was the most appropriate model for reproducing the multiplet structure, although the difference between the models in this (forsterite) case was rather small.

Cr^{4+}:åkermanite. The calculated multiplet energies and the theoretical absorption spectra in figure 9 obtained from the åkermanite models showed significant dependence on the size of the models. Comparing the result for model A with the experimental one shown in figure 9(d), we see that the calculated result reproduced the energy splitting of the $^3T_1(et_2)$ triplet term. However, the polarization dependence of the intensity was not adequately reproduced. In the theoretical spectrum for the $E \parallel c$ polarization, only the transition to the $^3A''_{(6)}[^3T_1(et_2)]$ state had a transition probability, but the transitions to the other two states in the same $^3T_1(et_2)$ triplet term also had obvious transition probabilities in the experimentally obtained spectrum. Furthermore, the transition probabilities for the transitions to the states in the $^3T_2(et_2)$ triplet term did not appear in the theoretical spectrum, in contrast to the case for the experimental spectrum in the NIR region. The difference between the results from models A and B were shown well in the insets. The calculated polarization dependence of model B came to agree with the experimentally obtained one. The effective Madelung potential accounted for the polarization dependence. When we focus on just the peak energy, we might be satisfied with the results obtained from the simplest model A. Our results indicated, however, that such a

simple model was no longer valid in this (åkermanite) case when we also took account of the transition probability. As in the forsterite case, the practical difference between the results of model B and the larger model C was small, although the covalency showed a difference. However, we can see the tendency that the result of model B gave the energy splittings of each of the multiplet terms as larger than those from model C. In model B, there was no space other than the CrO_4 tetrahedron to relax the difference in charge distribution, enhanced by the effective Madelung potential. On the other hand, in model C, the enhanced difference in charge distribution was relaxed by the first-shell cations, whose atomic orbitals mixed with the ligand O 2p orbitals.

Cr^{4+}:YSO. The calculated multiplet energies and the theoretical spectra obtained from the YSO models are shown in figure 10. The calculated multiplet energies of the excited triplet states and the peak energies obtained experimentally by Hömmerich *et al* [21] are summarized in table 9. The low C_1 symmetry produced energy splitting of every multiplet term. The energies obtained from models A and B agreed well with the experimentally obtained peak energies; on the other hand, the energies obtained from model C were rather overestimated. We ascribe the overestimation in model C to the overestimation of the mixing of the Y 4d orbital with the impurity-level MOs. Comparing with the results obtained from the forsterite and åkermanite models in figures 8 and 9, we consider that the $^3T_2(et_2)$ triplet term in YSO had the largest energy splitting in the NIR region. The theoretical and the experimental spectra showed polarization dependence, and the calculated intensity ratio depended on the model. The intensity ratio obtained from model A differed from that obtained from model B. This means that the effective Madelung potential in model B should not be neglected. The transition probability of the transition to the $^3A_{(6)}[^3T_1(et_2)]$ state was comparable to that of the transition to the $^3A_{(4)}[^3T_1(et_2)]$ and $^3A_{(5)}[^3T_1(et_2)]$ states in the spectra obtained from models A and B. On the other hand, the relative peak intensity related to the $^3A_{(6)}[^3T_1(et_2)]$ state was increased in the spectrum obtained from model C, making it closer to the experimentally obtained result. Here again, we consider that the largest model C is required to reproduce the intensity ratio. Including the wave functions of the first-shell-cation coordination polyhedra leads to better reproduction of the ligand field for C_1 symmetry. In previous semiempirical analyses, one might have considered approximating the symmetry as C_s, not as the exact C_1, to keep the number of adjustable parameters small. When we consider the transition probability, however, our result indicates that such a simplification is not a good approach.

Table 9. The calculated energies of the excited triplet states obtained from the YSO models, and Hömmerich's experimentally obtained peak energies (in cm^{-1}).

State	Model A	Model B	Model C	Experiment[a]
$^3A_{(1)}[^3T_2(et_2)]$	9031	9349	9698	9217
$^3A_{(2)}[^3T_2(et_2)]$	10017	10505	11414	10929
$^3A_{(3)}[^3T_2(et_2)]$	11310	11928	13407	12195
$^3A_{(4)}[^3T_1(et_2)]$	13186	13728	14281	13333
$^3A_{(5)}[^3T_1(et_2)]$	14401	15104	15989	14388
$^3A_{(6)}[^3T_1(et_2)]$	16546	16531	18257	16807
$^3A_{(7)}[^3T_1(t_2^2)]$	22202	22608	24250	
$^3A_{(8)}[^3T_1(t_2^2)]$	23252	24044	26769	
$^3A_{(9)}[^3T_1(t_2^2)]$	24444	25188	29339	

[a] Reference [21].

3.2.3. The relationship between the mixing of wave functions and the transition probability.
The analysed coefficients of the many-electron wave functions in equation (2) for the excited triplet states obtained from the forsterite, åkermanite, and YSO models C are shown in tables 10, 11, and 12, respectively. The values were normalized to unity, and the missing elements indicate zero. Every line in the tables means the composition of a state, and an off-diagonal element indicates that the wave function is mixed with those of the other states. In all of the results, the Slater determinants Φ_1–Φ_6 belonged to the et_2 electron configuration; on the other hand, the Slater determinants Φ_7–Φ_9 belonged to t_2^2 electron configuration.

Table 10. The analysed coefficients C_{ij} in the linear combination of Slater determinants Φ ($\Phi_1 = |a''_{(2)}(e), a'_{(3)}(t_2)|$, $\Phi_2 = |a'_{(1)}(e), a''_{(4)}(t_2)|$, $\Phi_3 = |a'_{(1)}(e), a'_{(5)}(t_2)|$, $\Phi_4 = |a'_{(1)}(e), a'_{(3)}(t_2)|$, $\Phi_5 = |a''_{(2)}(e), a'_{(5)}(t_2)|$, $\Phi_6 = |a''_{(2)}(e), a''_{(4)}(t_2)|$, $\Phi_7 = |a'_{(3)}(t_2), a''_{(4)}(t_2)|$, $\Phi_8 = |a'_{(3)}(t_2), a'_{(5)}(t_2)|$, $\Phi_9 = |a''_{(4)}(t_2), a'_{(5)}(t_2)|$, where $|\varphi_1, \varphi_2| = (1/\sqrt{2})\{\varphi_1(r_1)\varphi_2(r_2) - \varphi_2(r_1)\varphi_1(r_2)\}$ in equation (2), obtained from the forsterite model C.

State Ψ		(et₂) Φ_1	Φ_4	Φ_6	Φ_2	Φ_3	Φ_5	(t₂²) Φ_9	Φ_8	Φ_7
³T₂(et₂)	³A″₍₁₎	0.71			0.13		0.14			
	³A′₍₂₎		0.72	0.12		0.14				
	³A′₍₃₎			0.52		0.48				
³T₁(et₂)	³A″₍₄₎	0.24			0.46		0.20			0.10
	³A′₍₅₎		0.23	0.30		0.33			0.14	
	³A″₍₆₎	0.01			0.33		0.56	0.09		0.01
³T₁(t₂²)	³A″₍₇₎				0.02		0.07	0.85		0.05
	³A′₍₈₎		0.05	0.04		0.05			0.86	
	³A″₍₉₎	0.04			0.04		0.02	0.05		0.85

Garrett *et al* pointed out that the absorption spectra of the Cr^{4+}-doped forsterite and åkermanite showed a difference in polarization dependence, although the Cr sites in the two crystals possessed the same C_s symmetry [20]. In forsterite, the strongest peak in the visible region had $E \parallel a$ polarization, and the NIR region had different $E \parallel b$ or $E \parallel c$ polarizations. For åkermanite, on the other hand, the strongest peaks in the visible and the NIR regions had the same $E \parallel c$ polarization, which corresponded to the $E \parallel a$ polarization in forsterite. We found evidence for the difference in tables 10 and 11. In the tables, the states obtained from the forsterite and åkermanite models were classified into two groups, according to their symmetries. In forsterite, the ³A′ states were composed of the Slater determinants Φ_3, Φ_4, Φ_6, and Φ_8; on the other hand, the ³A″ states were composed of Φ_1, Φ_2, Φ_5, Φ_7, and Φ_9. In åkermanite, the ³A′ states were composed of Φ_1, Φ_3, Φ_6, and Φ_7; on the other hand, the ³A″ states were composed of Φ_2, Φ_4, Φ_5, Φ_8, and Φ_9. In general, transition from the ³A₂ state to ³T₂(et₂) state in T_d symmetry is electric dipole forbidden. However, some transitions become allowed when the states in the ³T₂(et₂) triplet term split and mix with the states in the ³T₁(et₂) triplet term, under the reduced symmetry. In the results from the forsterite model, the ³A″₍₆₎[³T₁(et₂)] state contained no apparent contribution from the Slater determinants Φ_1 and Φ_4, which were the primary components of the ³A″₍₁₎[³T₂(et₂)] and the ³A′₍₂₎[³T₂(et₂)] states, respectively. This absence of interaction is related to the fact that the polarizations of the strongest peak in the visible region and the apparent peaks in the NIR region could differ from each other. In the

Table 11. The analysed coefficients C_{ij} in the linear combination of Slater determinants Φ ($\Phi_1 = |a'_{(2)}(e), a'_{(3)}(t_2)|$, $\Phi_2 = |a''_{(1)}(e), a'_{(4)}(t_2)|$, $\Phi_3 = |a''_{(1)}(e), a''_{(5)}(t_2)|$, $\Phi_4 = |a''_{(1)}(e), a'_{(3)}(t_2)|$, $\Phi_5 = |a'_{(2)}(e), a''_{(5)}(t_2)|$, $\Phi_6 = |a'_{(2)}(e), a'_{(4)}(t_2)|$, $\Phi_7 = |a'_{(3)}(t_2), a'_{(4)}(t_2)|$, $\Phi_8 = |a'_{(3)}(t_2), a''_{(5)}(t_2)|$, $\Phi_9 = |a'_{(4)}(t_2), a''_{(5)}(t_2)|$, where $|\varphi_1, \varphi_2| = (1/\sqrt{2})\{\varphi_1(r_1)\varphi_2(r_2) - \varphi_2(r_1)\varphi_1(r_2)\}$) in equation (2), obtained from the åkermanite model C.

	State Ψ	(et$_2$)						(t$_2^2$)		
		Φ_1	Φ_4	Φ_3	Φ_2	Φ_6	Φ_5	Φ_8	Φ_7	Φ_9
$^3T_2(et_2)$	$^3A'_{(1)}$	0.78		0.14		0.07				
	$^3A''_{(2)}$		0.44		0.41		0.15			
	$^3A'_{(3)}$	0.02		0.59		0.39				
$^3T_1(et_2)$	$^3A''_{(4)}$		0.21		0.55	0.19				0.05
	$^3A'_{(5)}$	0.17		0.25		0.49			0.09	
	$^3A''_{(6)}$		0.34	.	0.01		0.63	0.01		
$^3T_1(t_2^2)$	$^3A''_{(7)}$						0.01	0.98		
	$^3A'_{(8)}$	0.03		0.02		0.04			0.91	
	$^3A''_{(9)}$		0.01		0.03		0.02			0.94

Table 12. The analysed coefficients C_{ij} in the linear combination of Slater determinants Φ ($\Phi_1 = |a_{(2)}(e), a_{(3)}(t_2)|$, $\Phi_2 = |a_{(1)}(e), a_{(4)}(t_2)|$, $\Phi_3 = |a_{(1)}(e), a_{(5)}(t_2)|$, $\Phi_4 = |a_{(1)}(e), a_{(3)}(t_2)|$, $\Phi_5 = |a_{(2)}(e), a_{(5)}(t_2)|$, $\Phi_6 = |a_{(2)}(e), a_{(4)}(t_2)|$, $\Phi_7 = |a_{(3)}(t_2), a_{(4)}(t_2)|$, $\Phi_8 = |a_{(3)}(t_2), a_{(5)}(t_2)|$, $\Phi_9 = |a_{(4)}(t_2), a_{(5)}(t_2)|$, where $|\varphi_1, \varphi_2| = (1/\sqrt{2})\{\varphi_1(r_1)\varphi_2(r_2) - \varphi_2(r_1)\varphi_1(r_2)\}$) in equation (2), obtained from the YSO model C.

	State Ψ	(et$_2$)						(t$_2^2$)		
		Φ_1	Φ_6	Φ_3	Φ_4	Φ_2	Φ_5	Φ_7	Φ_8	Φ_9
$^3T_2(et_2)$	$^3A_{(1)}$	0.70	0.08	0.02	0.16	0.01	0.02			
	$^3A_{(2)}$	0.04	0.47		0.03	0.43	0.03			
	$^3A_{(3)}$	0.10		0.75	0.07	0.07				0.01
$^3T_1(et_2)$	$^3A_{(4)}$	0.03	0.17	0.07	0.66	0.02	0.02	0.01	0.01	0.01
	$^3A_{(5)}$	0.09	0.25	0.15	0.04	0.41		0.02	0.02	0.01
	$^3A_{(6)}$	0.03			0.01	0.03	0.76	0.14	0.02	0.01
$^3T_1(t_2^2)$	$^3A_{(7)}$		0.01				0.17	0.67	0.03	0.11
	$^3A_{(8)}$		0.02			0.03		0.10	0.71	0.13
	$^3A_{(9)}$				0.02			0.06	0.21	0.71

theoretical spectrum in figure 8(c), we see that the strongest peak in the visible region had $E \parallel a$ polarization, corresponding to the $^3A''_{(6)}[^3T_1(et_2)]$ state. On the other hand, the apparent peaks in the NIR region had either $E \parallel b$ or $E \parallel c$ polarization, corresponding to the $^3A''_{(1)}[^3T_2(et_2)]$ and $^3A'_{(2)}[^3T_2(et_2)]$ states, respectively. Those results reproduced the experimentally obtained result. In the theoretical spectrum obtained from the åkermanite model in figure 9(c), the polarizations of the strongest peak in the visible region corresponding to the $^3A''_{(6)}[^3T_1(et_2)]$

state, and the primary peak in the NIR region corresponding to the $^3A''_{(2)}[^3T_2(et_2)]$ state, were for the same $E \parallel c$ polarization. The results agreed with the experimental one. In the analysed results in table 11, we see that the $^3A''_{(6)}[^3T_1(et_2)]$ state contained a large contribution from the Slater determinant Φ_4, which was the primary component of the $^3A''_{(2)}[^3T_2(et_2)]$ state. This interaction means that the transition to the $^3A''_{(6)}[^3T_1(et_2)]$ state gave its transition probability to the transition to the $^3A''_{(2)}[^3T_2(et_2)]$ state, and the two transitions had the transition probabilities for the same polarization.

In the result obtained from the YSO model C in table 12, we see that the many-electron wave functions of the triplet states were mixed with each other in a complex fashion, since the Cr site had the lowest C_1 symmetry. We could not extract any approximate matrix elements in a hypothetical higher symmetry, including C_s symmetry. We consider that this mixing under the C_1 symmetry is required when we consider the intensity ratio in the spectrum.

The transition probability of the transitions to the states in the $^3T_1(t_2^2)$ triplet term is solely derived from the mixing of the wave functions with those of the states in the et_2 electron configuration, since the two-electron excitation is originally forbidden. So the mixing of the wave functions of the states in the $^3T_1(t_2^2)$ triplet term with those of the states in the $^3T_1(et_2)$ triplet term produces the transition probability for the states in the $^3T_1(t_2^2)$ term. Comparing the analysed results in tables 10–12 and the theoretical spectra in figures 8–10, we find good correspondences between the mixing of the wave functions and the peak intensities for the states in the $^3T_1(t_2^2)$ triplet term. The larger the mixing, the stronger the corresponding peak. As regards Cr^{4+}:forsterite, Hazenkamp *et al* proposed an assignment from the experiments where the weak peak at $22\,700$ cm^{-1} for the $E \parallel c$ polarization originated from the $^3A''_{(0)}[^3A_2(e^2)] \rightarrow \, ^3A'_{(8)}[^3T_1(t_2^2)]$ transition. The theoretical spectrum in figure 8(c) showed a peak at $23\,204$ cm^{-1} for the same $E \parallel c$ polarization. The correspondence was good, and Hazenkamp's assignment is likely to be correct. Our calculated result further indicated that additional peaks with the same magnitudes of the oscillator strengths should exist around the same energy region also for $E \parallel a$ and $E \parallel b$ polarizations. Correspondingly, the three diagonal elements relating to the $^3T_1(t_2^2)$ triplet term were almost the same at 0.85. However, the agreement with the experimentally obtained spectrum is uncertain.

3.2.4. The reduction of two-electron repulsion. In the DVME method, the covalency, expressed by the proportions of the contribution of Cr 3d orbitals to impurity-level MOs, and the correlation-correction factor C, introduced by equation (7), are the reduction factors for the two-electron repulsion. Both of the factors are involved in equation (7), and are not adjustable parameters.

First, we see the reduction caused by the covalency. When the covalency becomes large, the effective spatial region where electrons move around spreads to reduce the repulsive energy between the electrons. In figure 11, the relationship between the proportion of Cr 3d orbitals and the two-electron integrals not multiplied by the factor C (=1) is plotted. In fact, the two-electron integrals had 140 combinations with different values, but only the most representative integrals, $\langle ij|kl \rangle = \langle 11|11 \rangle$, $\langle 22|22 \rangle$, $\langle 33|33 \rangle$, $\langle 44|44 \rangle$, and $\langle 55|55 \rangle$, in equation (7) were taken for simplicity. In the figure, not only the results obtained from models A, B, and C, but also a result obtained from a free-Cr^{4+}-ion model are shown. We find a good relationship between the covalency and the two-electron repulsion. This means that the proportion of the contribution of Cr 3d orbitals is a good parameter to use to simply evaluate the reduction caused by the covalency in the two-electron repulsion. We find that the MOs originating from the t_2 symmetry had larger covalency than the MOs originating from the e symmetry, and the two-electron repulsion was correspondingly reduced. The magnitude of the two-electron repulsion
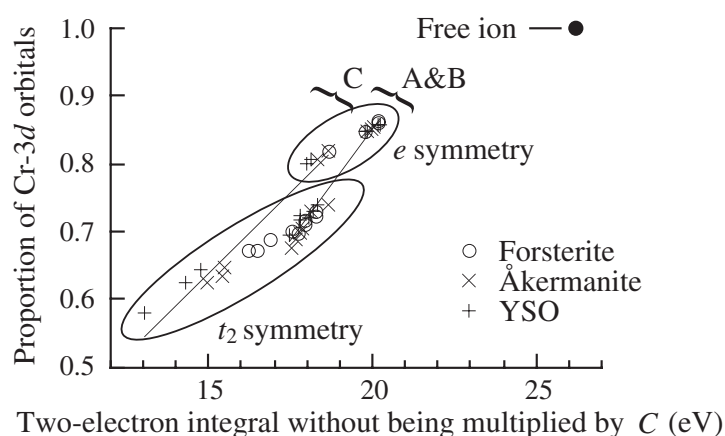
Figure 11. The relationship between the proportions of the contribution of Cr 3d orbitals and the two-electron integrals not multiplied by the correlation-correction factor C. The results A, B, and C were obtained from models A, B, and C, respectively, and a result obtained from the free-ion model is also shown.

in the models C being smaller than those in models A and B is ascribed to the participation of the first-shell-cation orbitals. When the first-shell-cation orbitals join the impurity-level MOs, the effective spatial region spreads, resulting in the reduction of the two-electron repulsion. The free-Cr^{4+}-ion model had no participation of orbitals other than the Cr 3d orbitals. The calculated value of the two-electron integral in the free-ion model was 26.2 eV, which was 1.3–2.0 times larger than the values obtained from models A, B, and C with ligand atoms.

The calculated values of another reduction factor, the correlation-correction factor C, are listed in table 13. Although the factor C can be originally calculated from first principles as explained in the method section, we obtained the factor C by fixing $\Delta \epsilon$ in equation (8) at an average value, 0.93 eV, for simplicity, through the calculations for models A, B, and C, but not the free-ion model. In models A, B, and C, we obtained values of the factor C in the range 0.60–0.70. The dependence of the factor C on the crystal was small, and was derived from the size of the models. We find a tendency for the magnitude of the factor C to decrease in the order of models C > A > B. This order is an opposite order to that for the magnitude of the proportions of the contribution of Cr 3d orbitals obtained in the previous section. This means that the correlation-correction factor C acted as a compensator for the reduction caused by the covalency, to keep the left-hand side of equation (8) constant. We multiplied the average values of the proportions of the contribution of Cr 3d orbitals and the correlation-correction factor C together, and the results are summarized in table 14. The calculated values of the resulting reduction factor lay in a small range, 0.47–0.50. This means that the resulting reduction factor is a good indicator with which to evaluate the reduction

Table 13. The calculated correlation-correction factor C, obtained from the forsterite, åkermanite, YSO, and free-ion models.

Model	Forsterite	Åkermanite	YSO	Free ion
A	0.64	0.63	0.62	
B	0.61	0.63	0.60	0.89
C	0.68	0.70	0.68	

Table 14. The (multiplied) reduction factor, obtained from the forsterite, åkermanite, and YSO models.

Model	Forsterite	Åkermanite	YSO
A	0.49	0.48	0.47
B	0.47	0.48	0.47
C	0.50	0.49	0.47

of two-electron repulsion, independently of the size of models. We had confirmed that the corresponding values of the two-electron integrals multiplied by the factor C also lay within a smaller range than the result in figure 11.

To consider the reduction of the two-electron repulsion directly, the values of the representative two-electron integrals multiplied by the factor C obtained from models C and the free-ion model are summarized in table 15. As mentioned before, we see good relationships between the two-electron integrals and the covalency. Although the forsterite and åkermanite possessed the same C_s symmetry, every integral had different values. In the traditional methods based on the ligand-field theory, such a difference has been neglected by reducing the integrals to just one Racah parameter B. Averaging the values of the two-electron integrals obtained from our models C, we obtained 11.3 eV as the value for solids. On the other hand, the value from the free-ion model was 23.2 eV. Accordingly, the ratio of the two-electron integrals in the ligand field to the free-ion value was 0.49. This ratio corresponds in meaning to the so-called nephelauxetic parameter, which is the ratio of the Racah parameter B for solids to the free-ion value. Many years ago, Jia *et al* reported a value of the Racah parameter B, 860 cm^{-1}, for Cr^{4+} in forsterite, derived from very simple semiempirical analysis using the Tanabe–Sugano diagram [16]. Since the Racah parameter of the free Cr^{4+} ion was reported as 1015 cm^{-1} [24], the Jia *et al* nephelauxetic parameter was 0.85. Later, Hazenkamp *et al* obtained a much smaller value of the Racah parameter B, 555 cm^{-1}, by an AOM calculation, and the value corresponded to the value of the nephelauxetic parameter 0.55 [23]. Although Jia *et al* and Hazenkamp *et al* determined those parameters by depending on the same assignment for the triplet states, their assumptions concerning the positions of the singlet states differed from each other, and they gave values of different magnitudes. Hazenkamp *et al* also obtained a value of the Racah parameter B of 540 cm^{-1} for Cr^{4+} in Ca_2GeO_4, which corresponds to the value of the nephelauxetic parameter 0.53. Reinen *et al* reported a similar small value, 0.47, from a similar AOM calculation [25]. For Cr^{4+}-doped $Y_3Al_5O_{12}$ (YAG), Eilers *et al*, Brik and Shchekoldin, and Riley *et al* independently obtained values of the Racah parameter B also by semiempirical analyses, and their nephelauxetic parameters lay in the range 0.42–0.51 [26–28].

Table 15. Representative two-electron integrals multiplied by the correlation-correction factor C, obtained from the forsterite, åkermanite, and YSO models C, and the free-ion model.

$\langle ij\vert kl\rangle$	Forsterite	Åkermanite	YSO	Free ion
$\langle 11\vert 11\rangle$	12.6	13.0	12.4	
$\langle 22\vert 22\rangle$	12.7	12.7	12.4	
$\langle 33\vert 33\rangle$	11.0	10.8	10.1	
$\langle 44\vert 44\rangle$	11.2	10.4	9.8	
$\langle 55\vert 55\rangle$	11.4	10.7	8.9	
Average	11.8	11.5	10.7	23.2

Our ratio 0.49 proves the invalidity of the large value of the nephelauxetic parameter proposed by Jia *et al*. We support the values at around 0.49 proposed by the others as having reasonable magnitudes. We have to stress, however, that the traditional nephelauxetic parameter is a very simple parameter based on an averaged single parameter for two-electron integrals. We stress also that reduction of the number of parameters is not appropriate, especially when discussing the transition probability.

4. Summary

The multiplet energies and the transition probabilities of tetrahedrally coordinated Cr^{4+} in the three silicate crystals forsterite, åkermanite, and YSO were calculated by the electronic structure calculation method, independently of ligand-field theory. The overall structures in the absorption spectra were reproduced, and that means that the structures were mainly produced by the tetrahedrally coordinated Cr^{4+}. The polarization dependence of the transition probability was reproduced well by the largest models with the first-shell-cation coordination polyhedra. The importance of the wave functions of the atoms outside the nearest ligand atoms indicates that the method will be applicable to examinations of electronic structures not only of single-ion systems but also of ion-pair systems and ion–vacancy systems. The ratio corresponding to the traditional nephelauxetic parameter was obtained as 0.49. The magnitudes of some values given recently in the literature were judged to be reasonable.

Acknowledgments

References

[1] Petričević V, Gayen S K, Alfano R R, Yamagishi K, Anzai H and Yamaguchi Y 1988 *Appl. Phys. Lett.* **52** 1040
   Petričević V, Gayen S K and Alfano R R 1988 *Appl. Phys. Lett.* **53** 2590
   Verdun H R, Thomas L M, Andrauskas D M, McCollum T and Pinto A 1988 *Appl. Phys. Lett.* **53** 2593
[2] Henderson B and Bartram R H 2000 *Crystal-Field Engineering of Solid-State Laser Materials* (Cambridge: Cambridge University Press) section 10.3.6
[3] Sugano S, Tanabe Y and Kamimura H 1970 *Multiplets of Transition-Metal Ions in Crystals* (New York: Academic)
[4] Xu Y-N and Ching W Y 1999 *Phys. Rev.* B **59** 10 530
[5] Xu Y-N, Ching W Y and Brickeen B K 2000 *Phys. Rev.* B **61** 1817
[6] Wissing K, Aramburu J A, Barriuso M T and Moreno M 1998 *Solid State Commun.* **108** 1001
[7] Deghoul F, Chermette H, Rogemond F, Moncorgé R, Stückl C and Daul C 1999 *Phys. Rev.* B **60** 2404
[8] Ogasawara K, Ishii T, Tanaka I and Adachi H 2000 *Phys. Rev.* B **61** 143
[9] Satoko C, Tsukada M and Adachi H 1978 *J. Phys. Soc. Japan* **45** 1333
[10] Slater J C, Wilson T M and Wood J H 1969 *Phys. Rev.* **179** 28
[11] Watanabe S and Kamimura H 1989 *Mater. Sci. Eng.* B **3** 313
[12] Slater J C 1974 *The Self-Consistent Field for Molecules and Solids, Quantum Theory of Molecules and Solids* (New York: McGraw-Hill) vol 4
[13] Smyth J R and Hazen R M 1973 *Am. Mineral.* **58** 588
[14] Malinovskii Y A and Panina Z V 1997 *Kristallografiya* **42** 1022 (Engl. Transl. 1997 *Crystallogr. Rep.* **42** 946)
[15] Maksimov B A, Ilyukhin V V, Kharitonov Y A and Belov N V 1970 *Kristallografiya* **15** 926 (Engl. Transl. 1971 *Sov. Phys.–Crystallogr.* **15** 806)
[16] Jia W, Liu H, Jaffe S, Yen W M and Denker B 1991 *Phys. Rev.* B **43** 5234
[17] Mulliken R S 1955 *J. Chem. Phys.* **23** 1833

[18] Ishii T, Ogasawara K, Adachi H and Tanaka I 2001 *J. Chem. Phys.* at press

[19] Verdún H R, Thomas L M, Andrauskas D M and Pinto A 1989 *OSA Proc. on Tunable Solid State Lasers (1989)* vol 5, ed M L Shand and H P Jenssen (Washington, DC: Optical Society of America) p 85

[20] Garrett M H, Chan V H, Jenssen H P, Whitmore M H, Sacra A, Singel D J and Simkin D J 1991 *OSA Proc. on Advanced Solid-State Lasers (1991)* vol 10, ed G Dubé and L Chase (Washington, DC: Optical Society of America) p 76

[21] Hömmerich U, Eilers H, Jacobsen S M, Yen W M and Jia W 1993 *J. Lumin.* **55** 293

[22] Koetke J, Kück S, Petermann K, Huber G, Cerullo G, Danailov M, Magni V, Qian L F and Svelto O 1993 *Opt. Commun.* **101** 195

[23] Hazenkamp M F, Güdel H U, Atanasov M, Kesper U and Reinen D 1996 *Phys. Rev.* B **53** 2367

[24] Bashkin S and Stoner Jr J O 1982 *Atomic Energy-Level and Grotrian Diagrams* vol 3 (Amsterdam: North-Holland)

[25] Reinen D, Kesper U, Atanasov M and Roos J 1995 *Inorg. Chem.* **34** 184

[26] Eilers H, Hömmerich U, Jacobsen S M, Yen W M, Hoffman K R and Jia W 1994 *Phys. Rev.* B **49** 15 505

[27] Brik M G and Shchekoldin D G 1998 *Opt. Spektrosk.* **84** 760 (Engl. Transl. 1998 *Opt. Spectrosc.* **84** 683)

[28] Riley M J, Krausz E R, Manson N B and Henderson B 1999 *Phys. Rev.* B **59** 1850